















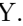








M. Wakai , S. Wallner , M.-Z. Wang , A. Warburton , M. Watanabe , S. Watanuki , C. Wessel ,
 E. Won , X. P. Xu , B. D. Yabsley , S. Yamada , W. Yan , J. Yelton , J. H. Yin , K. Yoshihara ,
 J. Yuan , Y. Yusa , L. Zani , V. Zhilich , J. S. Zhou , Q. D. Zhou , L. Zhu , and R. Žlebčik 

(The Belle II Collaboration)

(Dated: December 27, 2024)

We present a measurement of the branching fraction and fraction of longitudinal polarization of $B^0 \rightarrow \rho^+ \rho^-$ decays, which have two π^0 's in the final state. We also measure time-dependent CP violation parameters for decays into longitudinally polarized $\rho^+ \rho^-$ pairs. This analysis is based on a data sample containing $(387 \pm 6) \times 10^6$ $B\bar{B}$ pairs collected with the Belle II detector at the SuperKEKB asymmetric-energy e^+e^- collider in 2019-2022. We obtain $\mathcal{B}(B^0 \rightarrow \rho^+ \rho^-) = (2.88_{-0.22}^{+0.23+0.29}) \times 10^{-5}$, $f_L = 0.921_{-0.025}^{+0.024+0.017}$, $S = -0.26 \pm 0.19 \pm 0.08$, and $C = -0.02 \pm 0.12_{-0.05}^{+0.06}$, where the first uncertainties are statistical and the second are systematic. We use these results to perform an isospin analysis to constrain the CKM angle ϕ_2 and obtain two solutions; the result consistent with other Standard Model constraints is $\phi_2 = (92.6_{-4.8}^{+4.5})^\circ$.

I. INTRODUCTION

Charge-parity (CP) violation in the Standard Model (SM) is described by a single irreducible complex phase in the Cabibbo-Kobayashi-Maskawa (CKM) quark-mixing matrix [1, 2]. Measurements of CP asymmetries, mixing frequencies, and branching fractions (\mathcal{B}) of B hadron decays constrain the angles and sides of the CKM unitarity triangle (UT) [3, 4]. Although current measurements are consistent with the CKM picture of the SM, the precision still allows for $\mathcal{O}(10)\%$ non-SM contributions to the B^0 - \bar{B}^0 mixing amplitudes [5–10]. Hence, further improvement of experimental and theoretical knowledge of the UT can help to identify or constrain non-SM physics.

The angle ϕ_2 [11], which is defined in terms of CKM matrix elements as $\arg(-V_{td}V_{tb}^*/V_{ud}V_{ub}^*)$, is the least known angle of the UT; the current world average is $\phi_2 = (84.1_{-3.8}^{+4.5})^\circ$ [12]. We can determine the angle ϕ_2 by measuring the time-dependent CP asymmetry between B^0 and \bar{B}^0 decays proceeding via $b \rightarrow u\bar{u}d$ transitions.

In e^+e^- collisions at the $\Upsilon(4S)$ resonance, a quantum-entangled $B^0\bar{B}^0$ pair is produced via $e^+e^- \rightarrow \Upsilon(4S) \rightarrow B^0\bar{B}^0$. The probability to observe a B meson decaying into a CP eigenstate (B_{CP}) at proper time t_{CP} while the other B meson (B_{tag}) decays with flavor q ($q = +1$ for B^0 and $q = -1$ for \bar{B}^0) at proper time t_{tag} is given by

$$P(\Delta t, q) = \frac{e^{-|\Delta t|/\tau_{B^0}}}{4\tau_{B^0}} \left\{ 1 + q \left[S \sin(\Delta m_d \Delta t) - C \cos(\Delta m_d \Delta t) \right] \right\}, \quad (1)$$

where $\Delta t \equiv t_{CP} - t_{\text{tag}}$, τ_{B^0} is the lifetime of the B^0 meson, and Δm_d is the mass difference between the two B^0 mass eigenstates [12][13]. Here, S and C [14] are mixing-induced and direct CP violation parameters [15], respectively.

In B meson decays, the tree level $b \rightarrow u\bar{u}d$ process is the leading amplitude in $B \rightarrow \pi\pi$, $B \rightarrow \rho\pi$, $B \rightarrow \rho\rho$ and $B \rightarrow a_1\pi$ decays. This amplitude has a weak phase of ϕ_2 , including the phase from B^0 - \bar{B}^0 mixing. In addition, a $b \rightarrow d$ loop amplitude contributes to these decays at a

sub-leading level. This additional amplitude has a different weak phase from the tree amplitude and thus shifts the value of S from $\sin(2\phi_2)$ to $\sqrt{1-C^2} \sin(2\phi_2 + \Delta\phi_2)$. To estimate the effect of the loop amplitude and the shift $\Delta\phi_2$, an isospin analysis using the branching fractions and direct CP asymmetries in those charmless decays is used [16]. Such an analysis shows that $B^0 \rightarrow \rho^+ \rho^-$ [17] has a small contribution from the loop amplitude [18–24] and gives a more stringent constraint on ϕ_2 [25] than those resulting from $B \rightarrow \pi\pi$, $B \rightarrow \rho\pi$, and $B \rightarrow a_1\pi$ decays.

Since $B^0 \rightarrow \rho^+ \rho^-$ is the decay of a pseudo-scalar to two vector mesons, there are three helicity states of the ρ meson pair: longitudinal polarization (LP) and two transverse polarization (TP) states. The LP state is a pure CP -even eigenstate with helicity amplitude H_0 , while the TP states are mixtures of CP -even and CP -odd states with helicity amplitudes H_+ and H_- . The fraction of LP, defined as $f_L = |H_0|^2 / (|H_0|^2 + |H_+|^2 + |H_-|^2)$, is measured from the helicity angle distributions of ρ^\pm mesons. The distribution is given by

$$\frac{1}{\Gamma} \frac{d^2\Gamma}{d \cos \theta_{\rho^+} d \cos \theta_{\rho^-}} = \frac{9}{4} \left[\frac{1}{4} (1 - f_L) \sin^2 \theta_{\rho^+} \sin^2 \theta_{\rho^-} + f_L \cos^2 \theta_{\rho^+} \cos^2 \theta_{\rho^-} \right], \quad (2)$$

where θ_{ρ^\pm} is the angle in the rest frame of the ρ^\pm meson between the momentum of the π^0 from the $\rho^\pm \rightarrow \pi^\pm \pi^0$ decay and the B flight direction [12].

Previously, the Belle and BABAR experiments measured the branching fraction, f_L , and CP violation parameters for $B^0 \rightarrow \rho^+ \rho^-$. The results are summarized in Table I and confirm the dominance of LP. In this paper, we present a measurement of the branching fraction, the fraction of LP, and time-dependent CP asymmetries in $B^0 \rightarrow \rho^+ \rho^-$ using data from Belle II. The analysis is presented as follows. In Sec. II we describe the Belle II detector and data set used; in Sec. III we discuss event reconstruction and selection of signal candidates; in Sections IV and V we describe the fitting procedure and present the fit results; in Sec. VI we discuss systematic uncertainties; in Sec. VII we perform an isospin analysis

Table I. Recent precise measurements and world averages of the branching fraction, fraction of longitudinal polarization, and CP violation parameters for $B \rightarrow \rho^+ \rho^-$ decays. Note that both the Belle and *BABAR* experiments assume equal production of neutral and charged B meson pairs from $\Upsilon(4S)$ decay for their branching fraction measurements.

| Exp. | \mathcal{B} [10^{-5}] | f_L | S | C |
|-------------------|---------------------------------|-------------------------------------|----------------------------------|--------------------------|
| Belle [19] | $2.83 \pm 0.15 \pm 0.15$ | $0.988 \pm 0.012 \pm 0.023$ | $-0.13 \pm 0.15 \pm 0.05$ | $0.00 \pm 0.10 \pm 0.06$ |
| <i>BABAR</i> [18] | $2.55 \pm 0.21^{+0.36}_{-0.39}$ | $0.992 \pm 0.024^{+0.026}_{-0.013}$ | $-0.17 \pm 0.20^{+0.05}_{-0.06}$ | $0.01 \pm 0.15 \pm 0.06$ |
| PDG [12] | 2.77 ± 0.19 | $0.990^{+0.021}_{-0.019}$ | -0.14 ± 0.13 | 0.00 ± 0.09 |

to determine the angle ϕ_2 ; and in Sec. VIII we conclude.

II. DATA SET AND BELLE II DETECTOR

This measurement is based on $(365.4 \pm 1.7) \text{ fb}^{-1}$ [26] of data containing $(387 \pm 6) \times 10^6$ $B\bar{B}$ pairs collected on the $\Upsilon(4S)$ resonance. An additional sample of $42.7 \pm 0.2 \text{ fb}^{-1}$ accumulated at an energy 60 MeV below the $\Upsilon(4S)$ peak (off-resonance data), which is below the $B\bar{B}$ threshold, is used to study backgrounds. These data samples were taken with the Belle II detector [27] at the SuperKEKB asymmetric-energy e^+e^- collider [28] in 2019–2022.

The Belle II detector [27] has a cylindrical geometry and includes a two-layer silicon-pixel detector (PXD) surrounded by a four-layer double-sided silicon-strip detector (SVD) [29] and a 56-layer central drift chamber (CDC). These detectors reconstruct tracks of charged particles. Only one sixth of the second layer of the PXD was installed for the data analyzed here. The symmetry axis of these detectors, defined as the z axis, is almost coincident with the direction of the electron beam. Surrounding the CDC, which also provides dE/dx energy-loss measurements, is a time-of-propagation counter (TOP) [30] in the central region and an aerogel-based ring-imaging Cherenkov counter (ARICH) in the forward region. These detectors provide charged-particle identification. Surrounding the TOP and ARICH is an electromagnetic calorimeter (ECL) based on CsI(Tl) crystals that primarily provides energy and timing measurements for photons and electrons. Outside of the ECL is a superconducting solenoid magnet. The flux return of the magnet is instrumented with resistive-plate chambers and plastic scintillator modules to detect muons, K_L^0 mesons, and neutrons. The magnet provides a 1.5 T magnetic field that is oriented parallel to the z axis.

We use Monte Carlo (MC) simulated events to optimize selection criteria, calculate reconstruction efficiencies, and study sources of background. The $B\bar{B}$ samples are generated with EVTGEN [31]. Continuum $e^+e^- \rightarrow q\bar{q}$ ($q = u, d, s, c$) and $e^+e^- \rightarrow \tau^+\tau^-$ events are generated with KKMC [32]. The fragmentation of $q\bar{q}$ uses PYTHIA8 [33], and τ decays are simulated by TAUOLA [34]. Final state radiation is simulated by PHOTOS [35]. GEANT4 [36] is used to simulate the detector response to the passage of particles. Our simulation includes effects of beam-induced backgrounds [37, 38].

Both the data and simulated events are reconstructed using the Belle II software framework basf2 [39, 40].

III. RECONSTRUCTION AND EVENT SELECTION

Hadronic $B\bar{B}$ events are selected online using a hardware trigger based on total energy and charged-particle multiplicity, with an efficiency close to 100%. We subsequently reconstruct the $B^0 \rightarrow \rho^+ \rho^-$ decay from $\rho^+ \rightarrow \pi^+ \pi^0$ and $\pi^0 \rightarrow \gamma\gamma$. To reject misreconstructed tracks and charged particles from beam-induced background, we require that tracks be within the polar-angle acceptance of the CDC ($17^\circ < \theta < 150^\circ$) and have a distance-of-closest-approach to the e^+e^- interaction point (IP) of less than 0.5 cm in the transverse direction and less than 3.0 cm in the longitudinal (z) direction. We select π^\pm candidates using a charged particle identification (PID) ratio $\mathcal{L}_\pi/(\mathcal{L}_\pi + \mathcal{L}_K)$, where $\mathcal{L}_{\pi(K)}$ is the likelihood for a pion (kaon) hypothesis based mainly on information from the TOP and ARICH detectors, and, for low momentum tracks, the CDC. The pion-identification efficiency is 97% and the probability of a kaon being misidentified as a pion is 28%.

Photons are identified as clusters of ECL crystals having energy deposition above a threshold and not matched to tracks. We require minimum energies of 60 MeV and 90 MeV in the ECL barrel and endcap regions, respectively, where the barrel corresponds to the range $[32.2, 128.7]^\circ$ in polar angle, and the forward and backward endcaps correspond to the ranges $[12.4, 31.4]^\circ$ and $[130.7, 155.1]^\circ$, respectively. These minimum energy requirements suppress combinatorial background from low-energy photons. A tighter energy requirement is applied to the endcap region due to the higher level of beam-induced backgrounds in this region. To further suppress backgrounds, we require that there be at least two ECL crystals in the ECL cluster, and that the cluster time be within 200 ns of the collision time.

To distinguish photons from hadronic clusters or energy deposits split off from hadronic clusters, we train a fast boosted decision-tree (FBDT) [41] with the polar and azimuthal angles, energy, transverse momentum, and ten variables related to the cluster shape and its uncertainty. The classifier output used to distinguish correctly reconstructed photons is shown in Fig. 1. We choose a loose threshold on the FBDT output of $\mathcal{O}_P > 0.1$, which re-

moves 58% of mis-reconstructed photons while retaining 98% of signal photons.

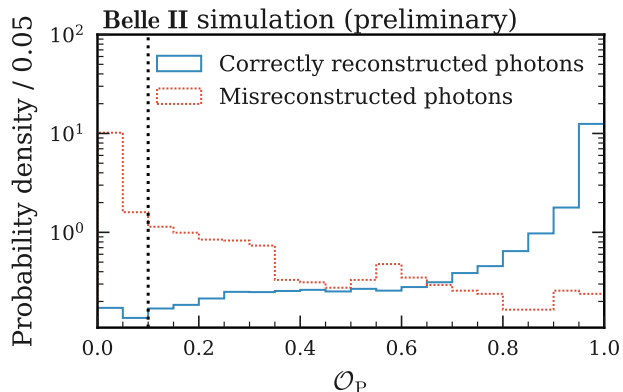


Fig. 1. Distribution of the FBDT classifier to distinguish correctly reconstructed photons (blue solid histogram) from hadronic clusters or splittings from charged-particle tracks (red dotted histogram) in simulation. The black dotted line corresponds to the threshold.

We reconstruct π^0 candidates from pairs of photon candidates with invariant mass in the range $120 \text{ MeV}/c^2 < m_{\gamma\gamma} < 150 \text{ MeV}/c^2$. The average mass resolution is approximately $6 \text{ MeV}/c^2$. Additionally, π^0 candidates must have momenta greater than $210 \text{ MeV}/c$. We also require that the difference between the polar angles of the photon momenta be less than 1.3 radians, and the difference between the azimuthal angles be less than 2.5 radians.

The selected π^\pm and π^0 candidates are combined to form ρ^\pm meson candidates, and we require $0.6 \text{ GeV}/c^2 < m_{\pi^\pm\pi^0} < 1.1 \text{ GeV}/c^2$. A B^0 candidate is reconstructed from pairs of $\rho^+\rho^-$ candidates. We fit the B^0 decay vertex with the TreeFit package [42], constraining the B^0 to originate from the IP. The resulting momenta of the decay products adjusted by the fit are used for further analysis. To further identify B^0 decays, we use two kinematic variables: the beam-energy-constrained mass

$M_{bc} \equiv \sqrt{E_{\text{beam}}^{*2}/c^4 - p_B^{*2}/c^2}$, and the energy difference $\Delta E \equiv E_B^* - E_{\text{beam}}^*$, where E_{beam}^* is the beam energy and E_B^* (p_B^*) is the energy (momentum) of the B meson, all evaluated in the center-of-mass (c.m.) frame. Candidate B mesons are required to satisfy $M_{bc} > 5.275 \text{ GeV}/c^2$ and $|\Delta E| < 0.15 \text{ GeV}$.

We determine the decay vertex of B_{tag} using the remaining tracks in the rest of the event (ROE). The tracks are required to have at least one hit in each of the PXD, SVD, and CDC detectors and have momenta greater than $50 \text{ MeV}/c$. Each track must originate from the IP and have impact parameters within 0.5 cm in the transverse direction and within 2.0 cm in the longitudinal direction. We determine an initial B_{tag} decay vertex from a χ^2 fit to all ROE tracks satisfying the above selection criteria; we then remove from the fit, one by one, tracks that contribute most to the χ^2 until the reduced χ^2 is less than

four. This minimization reduces the impact of displaced vertices due to intermediate charm mesons. We calculate Δt_l from the distance, Δl , between the B_{CP} vertex and the B_{tag} vertex along the $\Upsilon(4S)$ boost direction,

$$\Delta t_l = \frac{\Delta l}{c\beta\gamma_B}, \quad (3)$$

where $\beta\gamma = 0.28$ is the Lorentz boost of the $\Upsilon(4S)$ in the lab frame, and $\gamma_B = 1.002$ is the Lorentz boost of the B in the c.m. frame. The uncertainty on Δt_l , defined as $\sigma_{\Delta t}$, is estimated event-by-event by the vertex fitter. We reject poorly reconstructed events by requiring $|\Delta t_l| < 15 \text{ ps}$ and $\sigma_{\Delta t} < 2.00 \text{ ps}$. The quantity Δt_l can differ slightly from the Δt of Eq. 2, with the difference depending on the direction of the B^0 in the c.m. frame. We correct for this small effect in the same manner as done in Ref. [43]. The flavor of B_{tag} is identified by a flavor-tagging algorithm based on a graph neural network (GNN) that uses properties of charged particles in the ROE [44]. The GNN calculates the flavor q of B_{tag} and a quality factor r . The latter ranges from zero for no discriminating power to one for unambiguous flavor assignment. We do not impose a selection requirement on r ; rather, we divide the data into seven bins of r and use this binning in our subsequent fitting procedure. The bin boundaries are 0, 0.10, 0.25, 0.45, 0.60, 0.725, 0.875, and 1.

After the above reconstruction, we apply a selection $\cos\theta_{\rho^\pm} < 0.9$ to suppress combinatorial backgrounds from low-momentum π^0 's. The continuum background is suppressed using a TabNet classifier [45] that distinguishes the difference in topology between continuum events, which tend to be jet-like, and $B\bar{B}$ events, which tend to be spherical. We use the following 21 variables calculated in the c.m. frame as input parameters to the TabNet classifier: the cosine of the angle between the thrust axis [46] of the daughter particles of the B candidate and z -axis; the cosine of the angle between the thrust axes of the daughter particles of the B candidate and all other particles in the ROE; the cosine of the angle between the thrust axis of all particles in the event and the z -axis; the thrust value of the particles in the ROE; the cosine of the angle between the B momentum direction and the z -axis; the cosine of the angle, in the B rest frame, between the ρ^\pm direction and the boost direction of the B in the lab frame; and modified Fox-Wolfram moments [47, 48]. We train the classifier using a signal MC simulation sample with $f_L = 0.99$ and a $q\bar{q}$ background MC sample. The TabNet classifier removes more than 99% of $q\bar{q}$ background while retaining 38% of signal according to the simulation.

After the event selection and background suppression, 14.6% events have multiple candidates with, an average multiplicity of 2.3. In events with multiple candidates, we select the candidate with the smallest sum of three reduced- χ^2 values: two from the π^0 mass-constrained diphoton fits and one from the B -vertex fit. According to MC studies, the above criteria choose the correct signal

decay in 45% of multiple-candidate events for LP decays, and in 58% of such events for TP decays. These rates are a notable improvement over a random selection, for which the corresponding fractions are 37% and 46%.

The final selection criteria for photon energy, classifier output \mathcal{O}_P , angles between the momenta of the two photons, $m_{\gamma\gamma}$, π^0 momentum, PID, output of the TabNet classifier, and M_{bc} are optimized simultaneously by differential evolution [49] to maximize a figure-of-merit (FoM) $S/\sqrt{S+B}$, where S and B are the expected $B^0 \rightarrow \rho^+\rho^-$ signal and background yields, respectively, in a signal-enhanced region defined as $-0.08 \text{ GeV} < \Delta E < 0.04 \text{ GeV}$ and $0.6 \text{ GeV}/c^2 < m_{\pi^\pm\pi^0} < 0.9 \text{ GeV}/c^2$.

After the single candidate selection, the efficiencies for correctly reconstructed LP and TP signals calibrated with control samples as described in Section VI are 4.1% and 7.8%. These efficiencies include the branching fraction of $\pi^0 \rightarrow \gamma\gamma$. Some signal candidates are incorrectly reconstructed, e.g., they contain decay products of B_{tag} . These are referred to as self-crossfeed (SCF) events. Their Δt distributions depend on the number of correctly reconstructed charged pions. Thus, we divide SCF events into two categories. The first category (“SCF_a”) consists of decays in which both charged pions are correctly reconstructed, while the second category (“SCF_b”) consists of decays in which at least one of the charged pions is mis-reconstructed. For SCF_a events, the Δt_l distribution is unaffected, whereas for SCF_b events, the Δt_l distribution is smeared.

We check the consistency between data and simulation by reconstructing three control channels. The first is the decay chain $B^+ \rightarrow D^0\rho^+$, $D^0 \rightarrow K^-\pi^+\pi^0$, and $\rho^+ \rightarrow \pi^+\pi^0$, which is used to check the ΔE , $m_{\pi^\pm\pi^0}$, and $\cos\theta_{\rho^\pm}$ distributions. The same event selections as those used for the signal are applied to the π^\pm , π^0 , and ρ^\pm candidates. The second control channel is $B^0 \rightarrow D^{*-}\pi^+$, $D^{*-} \rightarrow \bar{D}^0\pi^-$, and $\bar{D}^0 \rightarrow K^+\pi^-$, which is used to check the TabNet classifier output and Δt distributions. The third control channel is $B^0 \rightarrow \rho^+\rho^-$ candidates in the M_{bc} sideband $5.24 \text{ GeV}/c^2 \leq M_{bc} \leq 5.26 \text{ GeV}/c^2$. This sample is used to check the background distributions.

IV. FIT STRATEGY AND MODELING

To measure \mathcal{B} , f_L , S , and C , we perform two unbinned maximum-likelihood fits. The first fit is an extended fit to the six observables ΔE , $m_{\pi^\pm\pi^0}$, $\cos\theta_{\rho^\pm}$, and \mathcal{T}_C , and determines the parameters \mathcal{B} and f_L . The observable \mathcal{T}_C is a transformed output of the TabNet classifier that is distributed uniformly between zero and one for LP signal events. Continuum background events, in contrast, peak at zero in \mathcal{T}_C . The second fit is to the observables Δt , q , and r , and determines S and C . For the latter fit, the signal probability is calculated event-by-event using the signal and background yields obtained from the first fit. The values for S and C are determined by an unbinned maximum likelihood fit to the Δt distributions for $q = +1$

and $q = -1$ events, in seven bins of r .

The components used in the fits are LP and TP signals, their SCF contributions, continuum, combinatorial and “peaking” $B\bar{B}$ backgrounds, and $e^+e^- \rightarrow \tau^+\tau^-$ ($\tau^+\tau^-$) events. Here, peaking $B\bar{B}$ backgrounds refer to charmless B decays that peak in the ΔE or $m_{\pi^\pm\pi^0}$ distributions. Other $B\bar{B}$ backgrounds are categorized as combinatorial $B\bar{B}$ backgrounds.

The likelihood for the signal-extraction fit is expressed as

$$\mathcal{L} = \frac{\prod_j e^{-N_j} n_{\text{tot}}}{n_{\text{tot}}!} \prod_{i=1}^{n_{\text{tot}}} \sum_j N_j \mathcal{P}_j(\Delta E, m_{\pi^+\pi^0}, m_{\pi^-\pi^0}, \cos\theta_{\rho^+}, \cos\theta_{\rho^-}, \mathcal{T}_C), \quad (4)$$

where N_j is the yield for component j , n_{tot} is the total number of events, and \mathcal{P}_j is the probability density function (PDF) for component j . The number of SCF events is proportional to the signal yield with a proportionality factor k . The values for the \mathcal{B} and f_L parameters are calculated from the LP and TP signal yields ($N_{\text{sig}}^{\text{LP(TP)}}$), using

$$\mathcal{B} = \frac{(N_{\text{sig}}^{\text{LP}}/\epsilon_{\text{LP}} + N_{\text{sig}}^{\text{TP}}/\epsilon_{\text{TP}})(f_{+-}/f_{00} + 1)}{2n_{B\bar{B}}}, \quad (5)$$

$$f_L = \frac{N_{\text{sig}}^{\text{LP}}/\epsilon_{\text{LP}}}{N_{\text{sig}}^{\text{LP}}/\epsilon_{\text{LP}} + N_{\text{sig}}^{\text{TP}}/\epsilon_{\text{TP}}}, \quad (6)$$

where ϵ_i are the signal efficiencies, and $n_{B\bar{B}}$ is the number of $B\bar{B}$ events produced. The factor f_{00} (f_{+-}) is the fraction of $B^0\bar{B}^0$ (B^+B^-) events in $\Upsilon(4S)$ decays. The value of the ratio f_{+-}/f_{00} is 1.052 ± 0.031 [50].

The likelihood for the time-dependent CP -asymmetry fit is

$$\mathcal{L}(\Delta t, \sigma_{\Delta t}, q, r) = \prod_{i=1}^{n_{\text{tot}}} \left[\sum_j f_j \mathcal{P}_j(\Delta t, \sigma_{\Delta t}, q, r) \right], \quad (7)$$

where $\mathcal{P}_j(\Delta t)$ is the PDF for component j , and f_j is the event-by-event component fraction calculated using the result of the signal-extraction fit. The fractions f_j are given by

$$f_j = \frac{N_j \mathcal{P}_j(\Delta E, m_{\pi^+\pi^0}, m_{\pi^-\pi^0}, \cos\theta_{\rho^+}, \cos\theta_{\rho^-}) \mathcal{P}_j(r)}{\sum_k N_k \mathcal{P}_k(\Delta E, m_{\pi^+\pi^0}, m_{\pi^-\pi^0}, \cos\theta_{\rho^+}, \cos\theta_{\rho^-}) \mathcal{P}_k(r)}, \quad (8)$$

where N_j is the number of events for the component j , $\mathcal{P}_j(\Delta E, m_{\pi^+\pi^0}, m_{\pi^-\pi^0}, \cos\theta_{\rho^+}, \cos\theta_{\rho^-})$ is the same PDF as in the signal-extraction fit, and we also include $\mathcal{P}_j(r)$, which is the PDF for r as a histogram with seven r bins. The PDFs for r are extracted from simulated samples. The variable $\sigma_{\Delta t}$ is utilized as a conditional variable in the resolution function of the Δt PDF. The various PDFs used in the fits are described below and summarized in Table II.

A. Signal-Extraction Fit

1. Correctly reconstructed Signal

The ΔE distribution is described by two bifurcated Gaussian functions with a common mean. The ρ^\pm lineshape is modeled by a relativistic Breit-Wigner (BW) function given by

$$A(m) = \frac{p_\pi}{m^2 - m_0^2 + im_0\Gamma(m)} \frac{F(p_\rho) F(p_\pi)}{F(p'_\rho) F(p'_\pi)}, \quad (9)$$

$$\Gamma(m) = \left(\frac{p_\pi}{p'_\pi}\right)^3 \left(\frac{m_0}{m}\right) \Gamma_0 \left[\frac{F(p_\pi)}{F(p'_\pi)}\right]^2, \quad (10)$$

where m_0 and Γ_0 are the peak position and width, respectively, of the ρ^\pm meson. The variable p_P is the momentum of the P particle in the rest frame of its parent particle, and p' is the momentum when the mass $m_{\pi^+\pi^0}$ equals m_ρ . The term $F(p)$ is the Blatt-Weisskopf form factor $F(p) = 1/\sqrt{1 + (Rp)^2}$, as described in Ref. [51]. Here, R is the meson radius parameter, which is set to 3 GeV^{-1} [31]. The PDF for the fit is obtained by $|A(m)|^2$. The parameters m_0 and Γ_0 are estimated by MC. They have different values from the PDG values [12] to account for the effects of detector resolution.

The \mathcal{T}_C distribution is parametrized by a linear function whose parameters are determined from a $B^0 \rightarrow D^{*-}\pi^+$ sample. The $\cos\theta_{\rho^\pm}$ distribution is modeled using a one-dimensional histogram template that depends on ΔE , to account for a correlation between $\cos\theta_{\rho^\pm}$ and ΔE . These templates are determined from MC-simulated samples. The ΔE and $m_{\pi^\pm\pi^0}$ peak positions and widths are calibrated using $B^\pm \rightarrow D^0\rho^\pm$ decays. The shape of the $\cos\theta_{\rho^\pm}$ distribution is also validated using the $B^\pm \rightarrow D^0\rho^\pm$ control sample. The signal yield is floated in the fit.

2. Signal Self-crossfeed

For self-cross-feed signal, the ΔE distributions are described by a bifurcated Gaussian function. The lineshape of $m_{\pi^\pm\pi^0}$ is described by the sum of a linear function and a relativistic BW function. The \mathcal{T}_C distribution is modeled by a linear function. A two-dimensional histogram template is used for $\cos\theta_{\rho^+}$ and $\cos\theta_{\rho^-}$, as these two observables are correlated. The same calibration factors as those used for correctly reconstructed signal are applied. The ratios of the SCF yields to the signal yields are fixed to the MC values: $k_{\text{SCF}_a}^{\text{LP}} = 0.19$, $k_{\text{SCF}_b}^{\text{LP}} = 0.16$ and $k_{\text{SCF}}^{\text{TP}} = 0.08$. The parameters for SCF modeling are determined from MC-simulated samples.

3. Continuum

For continuum events, the ΔE distribution is described by a quadratic function. Since continuum events also

include ρ resonances, the $m_{\pi^\pm\pi^0}$ distributions are modeled by a sum of a relativistic BW function and a linear function. As there are correlations in the ΔE - \mathcal{T}_C and $m_{\pi^\pm\pi^0}$ - $\cos\theta_{\rho^\pm}$ distributions, one-dimensional histogram templates depending on ΔE are adopted for modeling the \mathcal{T}_C distribution, and the $m_{\pi^\pm\pi^0}$ - $\cos\theta_{\rho^\pm}$ distributions are modeled in a similar way. These parameters are determined from the MC simulation samples. The same calibration parameters as those for signals are used for the $m_{\pi^\pm\pi^0}$ peak position and width. The continuum yield is free to vary.

A mis-modeling of the $\cos\theta_{\rho^\pm}$ distribution for $q\bar{q}$ MC samples is found in the M_{bc} sideband data. To improve the PDF modeling, we correct the π^\pm momentum distribution in the lab frame for the $q\bar{q}$ MC samples using sideband data, assuming that the $B\bar{B}$ background has the same distributions as the simulated sample. The correction factor for the $q\bar{q}$ distribution is consistent with what is obtained from studying off-resonance. The corrected $\cos\theta_{\rho^\pm}$ PDF is validated using sideband data and found to be consistent.

4. Combinatorial $B\bar{B}$ backgrounds

The ΔE and $m_{\pi^\pm\pi^0}$ distributions are both described by quadratic functions. The ΔE - \mathcal{T}_C and $m_{\pi^\pm\pi^0}$ - $\cos\theta_{\rho^\pm}$ distributions are modeled in the same way as continuum background. These parameters are obtained from MC simulated samples except for the ΔE shape. The ΔE shape parameters and the yield for combinatorial $B\bar{B}$ background are floated in the fit.

5. Peaking $B\bar{B}$ backgrounds

The decay of B mesons to all-pion final states or to final states with pions and a kaon could peak in the fit observables. The peaking backgrounds are modeled individually, as summarized in Table II. The branching fractions used are measured values when possible and are listed in Table III.

Most peaking backgrounds that are not yet measured are added together and treated as ‘‘rare peaking’’ backgrounds. Exceptions to this are modes with the same final state as $B^0 \rightarrow \rho^+\rho^-$, modes that are expected to have large branching fractions, and modes whose branching fractions can be estimated from similar modes, as described below. The modeling of these peaking backgrounds is summarized in Table II. The yield of the rare peaking background is floated in the signal extraction fit, while the relative contribution of an individual mode is fixed based on MC simulation.

The yields for the peaking backgrounds that have the same final state as $B^0 \rightarrow \rho^+\rho^-$, such as the decay chain $B^0 \rightarrow \rho^\pm\pi^\mp\pi^0$, $\rho^\pm \rightarrow \pi^\pm\pi^0$, $B^0 \rightarrow \pi^+\pi^-\pi^0\pi^0$ and $B^0 \rightarrow a_1^0\pi^0$, $a_1^0 \rightarrow \pi^+\pi^-\pi^0$, are floated in the signal-extraction fit. The effect of interference is not considered in the

nominal fit but is included as a systematic uncertainty. The $B^0 \rightarrow \pi^+\pi^-\pi^0$ decay contributes with the addition of a π from B_{tag} , and the PDFs are different from those of the combinatorial $B\bar{B}$ background and the signal. The yield of this component is floated in the fit.

The yields for $B^+ \rightarrow a_1^0\rho^+$ decays are fixed and also summarized in Table III. The branching fraction of this decay is unmeasured, so we assume it to be 2.5 times larger than the measured branching fraction of $B^\pm \rightarrow a_1^0\pi^\pm$, and assign a 100% uncertainty. For $B^0 \rightarrow a_1^\pm\rho^\mp$, since the 90% C.L. upper limit on the branching fraction is 6.1×10^{-5} , we take this branching fraction to be $(3 \pm 3) \times 10^{-5}$. The yields for $B \rightarrow a_1\rho$ decays are fixed and also summarized in Table III. For the modes peaking in ΔE or $m_{\pi^\pm\pi^0}$, these distributions are calibrated as described in Section IV A 1.

6. $\tau^+\tau^-$ background

The $\tau^+\tau^-$ background is suppressed by the selection with the TabNet classifier. The remaining events arise mostly from combinations of three decays: $\tau^- \rightarrow \pi^-\pi^+\pi^-\pi^0\nu_\tau$, $\tau^- \rightarrow \pi^-\pi^0\nu_\tau$, and $\tau^- \rightarrow \pi^-\pi^0\pi^0\nu_\tau$, which account for more than 90% of the $\tau^+\tau^-$ background. The ΔE distribution for $\tau^+\tau^-$ background is modeled by a quadratic function, and $m_{\pi^\pm\pi^0}$ is modeled by the sum of a relativistic BW function and a linear function. The \mathcal{T}_C distribution is modeled by an exponential function. The $\cos\theta_{\rho^\pm}$ distributions are described by one-dimensional histogram templates. These parameters are obtained from the MC simulation samples. In the fit, the yield is fixed to the expectation from MC simulation, 40.2 events.

B. Time-dependent CP-asymmetry fit

1. Correctly reconstructed Signal

Similar PDFs are used for the LP and TP signal events. Since the TP signal decay includes contributions from both CP -even and CP -odd states, our baseline fit assumes that CP -violating effects cancel out in the TP components; thus, in the PDF function for Δt , both S and C are set to zero. Possible nonzero values for the TP component are considered when evaluating systematic uncertainties.

The PDF for the Δt distribution of LP $B^0 \rightarrow \rho^+\rho^-$ decays is

$$\begin{aligned} \mathcal{P}(\Delta t, \bar{t}, q) = & \frac{1}{4\tau_{B^0}} \exp\left(\frac{-2\bar{t}}{\tau_{B^0}}\right) \left\{ 1 - q\Delta w_r + \right. \\ & q a_{\varepsilon,r}^{\text{tag}}(1 - 2w_r) \\ & + [q(1 - 2w_r) + a_{\varepsilon,r}^{\text{tag}}(1 - q\Delta w_r)] \\ & \left. [S \sin(\Delta m_d \Delta t) - C \cos(\Delta m_d \Delta t)] \right\}, \end{aligned} \quad (11)$$

where \bar{t} is the average of the B_{sig} and B_{tag} decay times, w_r is the wrong flavor-tag probability for bin r , Δw_r is the difference in wrong tag probabilities between B_{tag}^0 and \bar{B}_{tag}^0 for bin r , and $a_{\varepsilon,r}^{\text{tag}}$ is the asymmetry in B^0 and \bar{B}^0 flavor-tagging efficiencies for bin r [44]. We integrate out the \bar{t} dependence, which is related to the angular distribution of B_{sig} in the $\Upsilon(4S)$ rest frame [43].

The vertex resolution broadens the Δt distribution relative to the true distribution. To account for this broadening, we use the same resolution function as in Ref. [43] except for the f_{tail} modeling. The f_{tail} model is replaced with the sum of a constant and a bifurcated Gaussian having $\sigma_{\Delta t}$ as a parameter. The resolution function parameters are calibrated by fitting a $B^0 \rightarrow D^{*-}\pi^+$ control sample with flavor tagging parameters fixed to values from Ref. [44].

2. Signal Self-crossfeed

The correct CP violation parameters can be extracted from LP SCF_a events, as the B decay position (determined from the trajectories of the two charged pions) is correctly reconstructed. Thus, the Δt PDF for correctly reconstructed signal is used for the LP SCF_a events with shared CP violation parameters. In contrast, the Δt distribution for the LP SCF_b events is biased due to the contamination of charged tracks from B_{tag} . The Δt PDF is modeled using the PDF for correctly reconstructed LP signal with an effective lifetime determined from MC-simulated samples.

For the TP SCF events, SCF_a and SCF_b are modeled with the same Δt PDF. This PDF is the same as that used for the correctly reconstructed TP signal but with an effective lifetime determined from simulation.

3. Continuum

The Δt PDF for continuum background is modeled by the sum of two Gaussian functions with mean parameters set to zero. The standard deviations and relative fractions of the Gaussians are determined from off-resonance data.

4. Combinatorial $B\bar{B}$ backgrounds

The Δt PDF for combinatorial $B\bar{B}$ backgrounds is modeled by an exponential function with an effective lifetime convolved with the resolution function. The effective lifetime is determined to be 1.39 ± 0.02 ps from the simulation. The effective lifetime for the combinatorial $B\bar{B}$ backgrounds is determined from the sideband data, which is consistent with the MC result.

Table II. Summary of fit models for each event type. BG: bifurcated-Gaussian, DBG: sum of two bifurcated-Gaussians sharing a common mean, DG: sum of two Gaussians sharing a common mean, BW: Breit-Wigner distribution, P_i : i th order polynomial function, and exp: an exponential function. The notation $|_X$ indicates that the correlation with X is considered. The superscript CP indicates the inclusion of a CP asymmetry term, and the subscript τ_{B^0} or τ_{eff} denote the B^0 lifetime or an effective lifetime determined from MC simulation. The factor \mathcal{R} represents a resolution function. The yields for the processes in the upper half of the Table are floated while the yields for processes in the lower half are fixed.

| Process | ΔE | $m_{\pi^\pm\pi^0}$ | \mathcal{T}_C | $\cos\theta_{\rho^\pm}$ | Δt |
|---|-------------|-----------------------------------|----------------------|-----------------------------------|---|
| LP signal | DBG | BW | P_1 | Template $ \Delta E$ | $\exp_{\tau_{B^0}^{CP}} \otimes \mathcal{R}$ |
| LP SCF _a | BG | BW + P_1 | P_1 | Template $ \cos\theta_{\rho^\pm}$ | $\exp_{\tau_{B^0}^{CP}} \otimes \mathcal{R}$ |
| LP SCF _b | BG | BW + P_1 | P_1 | Template $ \cos\theta_{\rho^\pm}$ | $\exp_{\tau_{\text{eff}}^{CP}} \otimes \mathcal{R}$ |
| TP signal | DBG | BW | P_1 | Template $ \Delta E$ | $\exp_{\tau_{B^0}} \otimes \mathcal{R}$ |
| TP SCF | BG | BW + P_1 | P_1 | Template $ \cos\theta_{\rho^\pm}$ | $\exp_{\tau_{\text{eff}}} \otimes \mathcal{R}$ |
| $q\bar{q}$ | P_2 | BW + P_1 | Template $ \Delta E$ | Template $ \cos\theta_{\rho^\pm}$ | DG |
| $B\bar{B}$ | P_2 | P_2 | Template $ \Delta E$ | Template $ \cos\theta_{\rho^\pm}$ | $\exp_{\tau_{\text{eff}}} \otimes \mathcal{R}$ |
| $B^0 \rightarrow \rho^\pm \pi^\mp \pi^0$ | DBG | Template $ \cos\theta_{\rho^\pm}$ | Template $ \Delta E$ | Template $ \cos\theta_{\rho^\pm}$ | $\exp_{\tau_{\text{eff}}} \otimes \mathcal{R}$ |
| $B^0 \rightarrow \pi^+ \pi^- \pi^0 \pi^0$ | DBG | P_1 | Template $ \Delta E$ | Template $ \Delta E$ | $\exp_{\tau_{\text{eff}}} \otimes \mathcal{R}$ |
| $B^0 \rightarrow a_1^0 \pi^0$ | DBG | Template $ \cos\theta_{\rho^\pm}$ | Template $ \Delta E$ | Template $ \cos\theta_{\rho^\pm}$ | $\exp_{\tau_{\text{eff}}} \otimes \mathcal{R}$ |
| $B^0 \rightarrow \pi^+ \pi^- \pi^0$ | P_2 | BW + P_1 | Template $ \Delta E$ | Template | $\exp_{\tau_{\text{eff}}} \otimes \mathcal{R}$ |
| rare peaking backgrounds | DBG | BW + P_1 | P_1 | Template $ \cos\theta_{\rho^\pm}$ | $\exp_{\tau_{\text{eff}}} \otimes \mathcal{R}$ |
| $\tau^+ \tau^-$ | P_2 | BW + P_1 | exp + P_1 | Template | DG |
| $B^0 \rightarrow \rho^\pm \pi^\mp$ | P_2 | BW + P_1 | P_1 | Template $ \cos\theta_{\rho^\pm}$ | $\exp_{\tau_{\text{eff}}} \otimes \mathcal{R}$ |
| $B^0 \rightarrow a_1^\pm \pi^\mp$ | DBG | Template $ \cos\theta_{\rho^\pm}$ | P_1 | Template | $\exp_{\tau_{\text{eff}}} \otimes \mathcal{R}$ |
| $B^0 \rightarrow a_1^\pm \rho^\mp$ | exp + P_1 | BW + P_1 | Template $ \Delta E$ | Template | $\exp_{\tau_{\text{eff}}} \otimes \mathcal{R}$ |
| $B^0 \rightarrow K^{*+} \rho^-$ | DBG | Template $ \cos\theta_{\rho^\pm}$ | P_1 | Template | $\exp_{\tau_{\text{eff}}} \otimes \mathcal{R}$ |
| $B^0 \rightarrow K_0^*(1430)^+ \rho^-$ | P_2 | Template $ \cos\theta_{\rho^\pm}$ | P_1 | Template | $\exp_{\tau_{\text{eff}}} \otimes \mathcal{R}$ |
| $B^+ \rightarrow \rho^+ \pi^0$ | P_2 | Template $ \cos\theta_{\rho^\pm}$ | P_1 | Template $ \cos\theta_{\rho^\pm}$ | $\exp_{\tau_{\text{eff}}} \otimes \mathcal{R}$ |
| $B^+ \rightarrow \rho^+ \rho^0$ | DBG | BW + P_1 | P_1 | Template $ \cos\theta_{\rho^\pm}$ | $\exp_{\tau_{\text{eff}}} \otimes \mathcal{R}$ |
| $B^+ \rightarrow a_1^0 \pi^+$ | DBG | BW + P_1 | P_1 | Template $ \cos\theta_{\rho^\pm}$ | $\exp_{\tau_{\text{eff}}} \otimes \mathcal{R}$ |
| $B^+ \rightarrow a_1^+ \pi^0$ | DBG | BW + P_1 | P_1 | Template | $\exp_{\tau_{\text{eff}}} \otimes \mathcal{R}$ |
| $B^+ \rightarrow a_1^0 \rho^+$ | exp + P_1 | BW + P_1 | Template $ \Delta E$ | Template | $\exp_{\tau_{\text{eff}}} \otimes \mathcal{R}$ |
| $B^+ \rightarrow K^+ \pi^- \pi^+$ | P_2 | BW + P_1 | P_1 | Template | $\exp_{\tau_{\text{eff}}} \otimes \mathcal{R}$ |
| $B^+ \rightarrow K_0^*(1430)^+ \pi^0$ | BG | P_1 | P_1 | Template $ \cos\theta_{\rho^\pm}$ | $\exp_{\tau_{\text{eff}}} \otimes \mathcal{R}$ |

5. Peaking $B\bar{B}$ backgrounds

The Δt PDFs for each peaking background and rare peaking background are modeled with the same functional form as the combinatorial $B\bar{B}$ backgrounds but with a mode-specific effective lifetime as determined from MC-simulated samples. The CP violation parameters are fixed to world average values if measurements are available; or fixed to zero otherwise. The CP violation parameters used for the fit are summarized in Table IV.

6. $\tau^+ \tau^-$ background

The Δt PDF is modeled by a sum of two Gaussian functions. The means, standard deviations, and relative fractions are fixed to values from MC simulation.

7. Validation of Δt PDF

To validate the Δt resolution function, we use a $B^0 \rightarrow D^{*-} \pi^+$ control sample to fit for parameters τ_{B^0} and Δm_d . We set $S = 0$, $C = -1$, and $q = q_{\text{tag}} \cdot q_{\text{sig}}$, where q_{tag} and q_{sig} represent the flavors of the tag-side and signal side. The results are $\tau_{B^0} = 1.523 \pm 0.033$ ps and $\Delta m_d = 0.507 \pm 0.017$ ps $^{-1}$, where the uncertainties are statistical. We further check the Δt resolution function using flavor-untagged $B^0 \rightarrow \rho^+ \rho^-$ candidates and obtain $\tau_{B^0} = 1.41 \pm 0.13$ ps, which is also consistent with the world average value. These results are in excellent agreement with the world average values of $\tau_{B^0} = 1.517 \pm 0.004$ ps and $\Delta m_d = 0.5069 \pm 0.0019$ ps $^{-1}$ [12]. We also perform a time-dependent CP -asymmetry fit to $B^0 \rightarrow \rho^+ \rho^-$ candidates, randomly assigning flavor ± 1 to q . We obtain $S = -0.070 \pm 0.186$ and $C = -0.079 \pm 0.121$, which are consistent with zero as expected.

Table III. Peaking backgrounds from B^0 and B^+ decays, their branching fractions, and the number of events expected in 365.4 fb^{-1} of data. We use PDG values [12] for modes that have been measured. For modes that are unmeasured, we assign a 100% uncertainty to the estimated branching fractions.

| Decay mode | \mathcal{B} [10^{-6}] | N_{bg} |
|--|-----------------------------|-----------------|
| $B^0 \rightarrow \rho^\pm \pi^\mp$ | 23.0 ± 2.3 | 5.0 |
| $B^0 \rightarrow a_1^\pm \pi^\mp$ | 26 ± 5 | 8.1 |
| $B^0 \rightarrow a_1^\pm \rho^\mp$ | 30 ± 30 | 8.7 |
| $B^0 \rightarrow K^{*+} \rho^-$ | 10.3 ± 2.6 | 9.9 |
| $B^0 \rightarrow K_0^*(1430)^+ \rho^-$ | 28 ± 12 | 10.2 |
| $B^+ \rightarrow \rho^+ \pi^0$ | 10.9 ± 1.4 | 39.0 |
| $B^+ \rightarrow \rho^+ \rho^0$ | 24.0 ± 1.9 | 21.1 |
| $B^+ \rightarrow a_1^0 \pi^+$ | 20 ± 6 | 5.5 |
| $B^+ \rightarrow a_1^+ \pi^0$ | 26 ± 7 | 16.5 |
| $B^+ \rightarrow a_1^0 \rho^+$ | 50 ± 50 | 18.2 |
| $B^+ \rightarrow K^+ \pi^- \pi^+$ | 51 ± 29 | 1.2 |
| $B^+ \rightarrow K_0^*(1430)^+ \pi^0$ | $11.9_{-2.3}^{+2.0}$ | 4.3 |

Table IV. CP violation parameters of the peaking backgrounds used for the fit. Here, A_{CP} is the direct CP violation parameter for flavor specific modes. We use PDG values for the measured modes [12] while we assign $\pm 50\%$ uncertainties for the decays that are not measured yet.

| Decay mode | S | C | A_{CP} |
|---|-----------------|------------------|------------------|
| $B^0 \rightarrow \rho^\pm \pi^\mp \pi^0$ | 0.0 ± 0.5 | 0.0 ± 0.5 | — |
| $B^0 \rightarrow \pi^+ \pi^- \pi^0 \pi^0$ | 0.0 ± 0.5 | 0.0 ± 0.5 | — |
| $B^0 \rightarrow a_1^0 \pi^0$ | 0.0 ± 0.5 | 0.0 ± 0.5 | — |
| $B^0 \rightarrow \pi^+ \pi^- \pi^0$ | 0.0 ± 0.5 | 0.0 ± 0.5 | — |
| $B^0 \rightarrow K_S^0 \pi^0 \pi^0$ | 0.89 ± 0.30 | -0.21 ± 0.20 | — |
| $B^0 \rightarrow \rho^\pm \pi^\mp$ | 0.05 ± 0.07 | -0.03 ± 0.07 | — |
| $B^0 \rightarrow a_1^\pm \pi^\mp$ | -0.2 ± 0.4 | -0.05 ± 0.11 | — |
| $B^0 \rightarrow a_1^\pm \rho^\mp$ | 0.0 ± 0.5 | 0.0 ± 0.5 | — |
| $B^0 \rightarrow K^{*+} \rho^-$ | — | — | 0.21 ± 0.15 |
| $B^0 \rightarrow K_0^*(1430)^+ \rho^-$ | — | — | 0.0 ± 0.5 |
| $B^+ \rightarrow \rho^+ \pi^0$ | — | — | 0.03 ± 0.10 |
| $B^+ \rightarrow \rho^+ \rho^0$ | — | — | -0.05 ± 0.05 |
| $B^+ \rightarrow a_1^0 \pi^+$ | — | — | 0.0 ± 0.5 |
| $B^+ \rightarrow a_1^+ \pi^0$ | — | — | 0.0 ± 0.5 |
| $B^+ \rightarrow a_1^0 \rho^+$ | — | — | 0.0 ± 0.5 |

V. FIT RESULTS

We first measure the branching fraction and fraction of longitudinal polarization. For this fit, we float \mathcal{B} and f_L as well as the yields of combinatorial $B\bar{B}$, $q\bar{q}$, $B^0 \rightarrow \rho^\pm \pi^\mp \pi^0$, $B^0 \rightarrow \pi^+ \pi^- \pi^0 \pi^0$, $B^0 \rightarrow a_1^0 \pi^0$, $B^0 \rightarrow \pi^+ \pi^- \pi^0$, rare peaking backgrounds, and the ΔE shape for combinatorial $B\bar{B}$ backgrounds. Figure 2 shows projections of the fit result overlaid on the ΔE , $m_{\pi^\pm \pi^0}$, \mathcal{T}_C , and $\cos \theta_{\rho^\pm}$ distributions. The fit result and the data are in

good agreement. We obtain

$$\mathcal{B}(B^0 \rightarrow \rho^+ \rho^-) = (2.88_{-0.22}^{+0.23}) \times 10^{-5}, \quad (12)$$

$$f_L = 0.921_{-0.025}^{+0.024}, \quad (13)$$

where the uncertainties are statistical only. The statistical correlation is -0.11 . The measured fraction of LP is slightly lower than, but consistent within 2σ with the world average. The signal and background yields determined by the fit are summarized in Table V.

Table V. Fit results for signal and background yields. The uncertainties are statistical.

| | N |
|---|--------------------------|
| LP signal | $436.3_{-33.5}^{+34.2}$ |
| TP signal | $65.4_{-22.6}^{+24.3}$ |
| LP signal (SCF) | $151.0_{-11.6}^{+11.9}$ |
| TP signal (SCF) | $5.6_{-1.8}^{+1.9}$ |
| $q\bar{q}$ | $1410.2_{-75.7}^{+76.5}$ |
| Combinatorial $B\bar{B}$ | $849.2_{-72.3}^{+73.3}$ |
| $B^0 \rightarrow \rho^+ \pi^- \pi^0$ | $44.9_{-91.9}^{+93.3}$ |
| $B^0 \rightarrow \pi^+ \pi^- \pi^0 \pi^0$ | $-98.0_{-60.2}^{+62.2}$ |
| $B^0 \rightarrow \pi^+ \pi^- \pi^0$ | $-1.2_{-15.9}^{+18.8}$ |
| $B^0 \rightarrow a_1^0 \pi^0$ | $32.0_{-26.5}^{+28.6}$ |
| Rare peaking backgrounds | $-31.9_{-42.9}^{+45.3}$ |

We subsequently perform a second fit to extract the CP violation parameters. Figure 3 shows the Δt distributions with the fit result superimposed. The results are

$$S = -0.26 \pm 0.19 \quad (14)$$

$$C = -0.02 \pm 0.12, \quad (15)$$

where the uncertainties are statistical only and include uncertainties due to statistical uncertainties in \mathcal{B} and f_L . These are obtained by varying \mathcal{B} and f_L by their uncertainties, accounting for their correlation. The statistical correlation is -0.06 .

VI. SYSTEMATIC UNCERTAINTIES

We consider systematic uncertainties in \mathcal{B} , f_L , S , and C , which are listed in Tables VI and Table VII. The major sources of systematic uncertainties are the π^0 efficiency for \mathcal{B} , fit bias and data-MC mis-modeling for f_L , possible CP asymmetries in backgrounds, and the resolution function for S and C .

A. Signal-Extraction Fit

Table VI summarizes the statistical and systematic uncertainties of the signal-extraction fit. The signal efficiency is determined based on the MC-simulated samples, corrected using the data-MC ratio of the tracking,

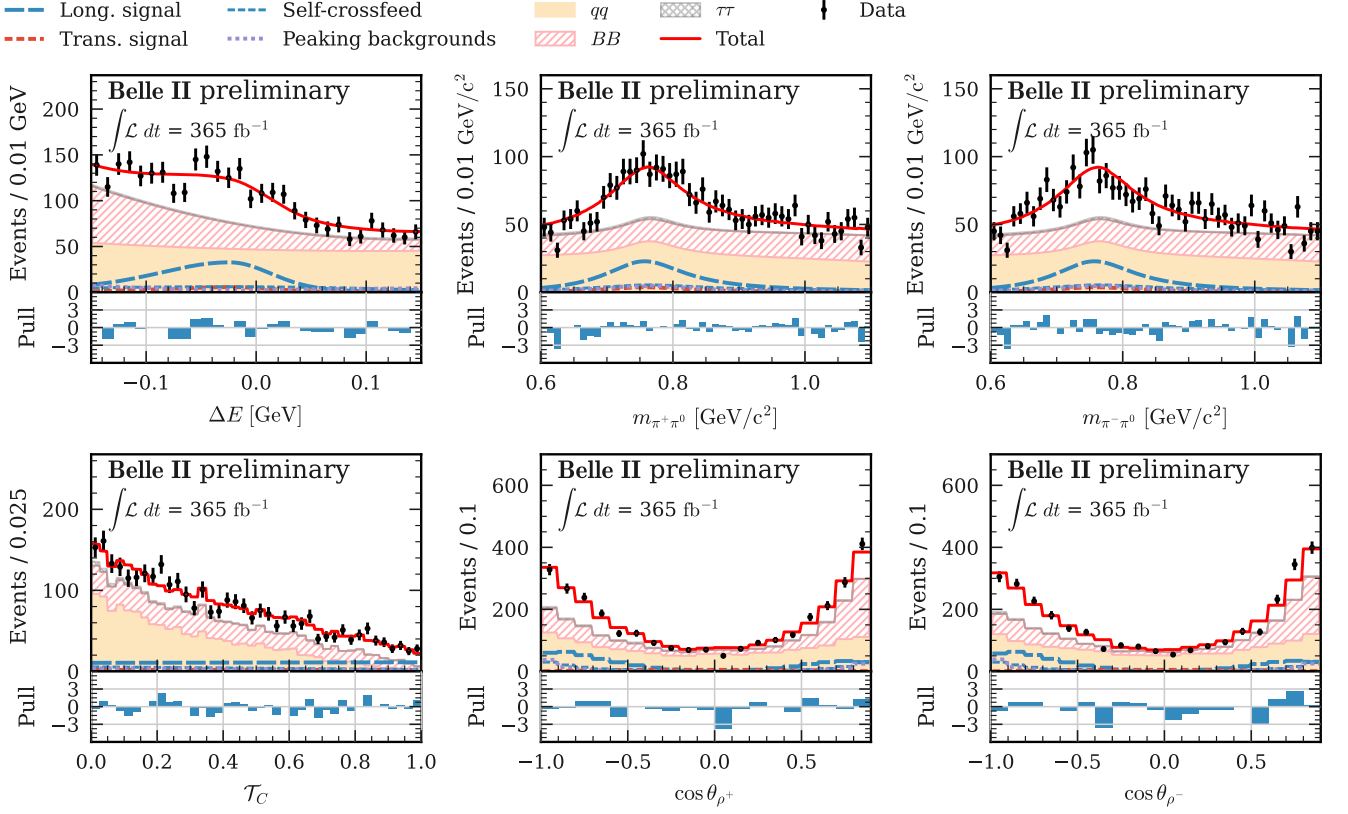


Fig. 2. Distributions for ΔE (top left), $m_{\pi^\pm\pi^0}$ (top center, top right), \mathcal{T}_C (bottom left), and $\cos\theta_{\rho^\pm}$ (bottom center, bottom right). The points with error bars represent the data, the solid red curves show the sum of all contributions, the long-dashed blue curves show the LP signal, the short-dashed red curves show the TP signal, the short-dashed blue curves show the sum of LP and TP SCF, the dotted purple curves represent peaking backgrounds. The hatched red histograms show the $B\bar{B}$ background, the shaded (orange) histograms show the continuum events, and the cross-hatched (black) histograms represent the $\tau^+\tau^-$ background.

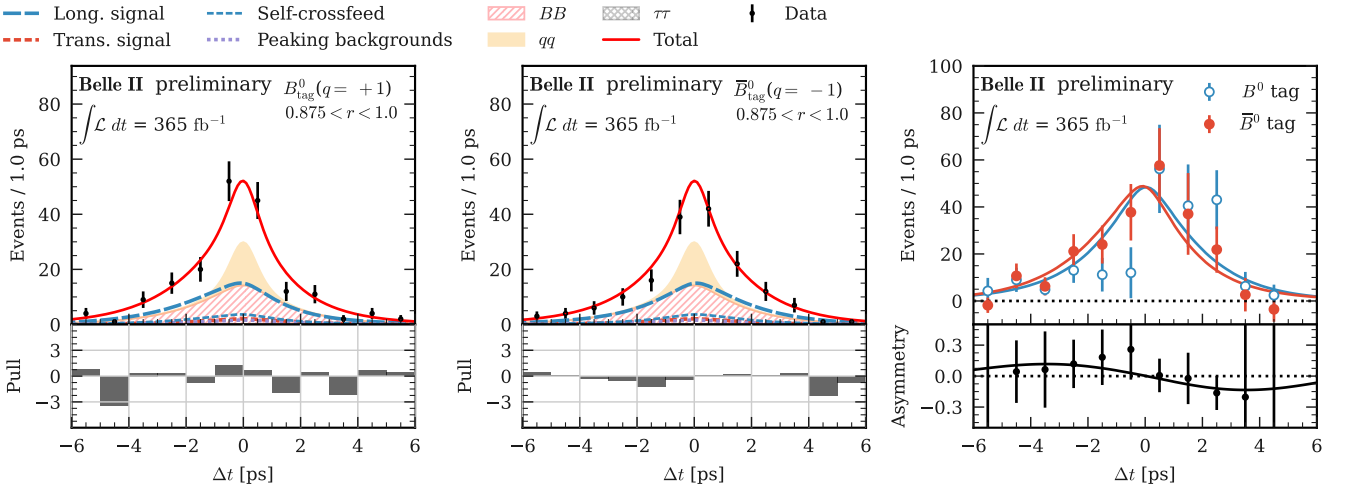


Fig. 3. Distributions for Δt of B_{tag}^0 in $0.875 < r < 1.0$ (left), Δt of \bar{B}_{tag}^0 in $0.875 < r < 1.0$ (center), and background-subtracted asymmetry using the $sPlot$ technique [52]. The points with error bars represent the data and the curves show the fit result. The sWeights are calculated using ΔE , $m_{\pi^\pm\pi^0}$, $\cos\theta_{\rho^\pm}$, and qr .

π^0 , PID, and TabNet classifier efficiencies. These ratios are evaluated using control samples.

The uncertainty of charged track finding is evaluated using $e^+e^- \rightarrow \tau^+\tau^-$ data, in which one τ decays as $\tau^+ \rightarrow \ell^+\nu_\ell\bar{\nu}_\tau$ and the other decays as $\tau^+ \rightarrow \pi^-\pi^+\pi^-\nu_\tau$. The data-MC ratios of the tracking efficiency are 0.9999 ± 0.0029 for the LP signal and 0.9999 ± 0.0027 for the TP signal. The neutral-pion efficiency is studied using $D^0 \rightarrow K^-\pi^+\pi^0$, $D^0 \rightarrow K^-\pi^+$, and $B^- \rightarrow D^{*0}\pi^-$ followed by $D^{*0} \rightarrow D^0\pi^0$ and $D^0 \rightarrow K^-\pi^+$. The data-MC ratios of the efficiency are 1.011 ± 0.039 for the LP signal and 1.040 ± 0.038 for the TP signal. We obtain a systematic uncertainty associated with the charged-pion identification efficiency using pions from the decay chain $D^{*+} \rightarrow D^0\pi^+$ followed by $D^0 \rightarrow K^-\pi^+$. The data-MC ratios of the charged-pion identification efficiency are 0.9946 ± 0.0004 for the LP signal and 0.9934 ± 0.0004 for the TP signal. The efficiency of the TabNet classifier and the shape of \mathcal{T}_C are evaluated using a $B^0 \rightarrow D^{*-}\pi^+$ control sample. The data-MC ratio of the efficiency is 1.082 ± 0.031 . The systematic uncertainties associated with the efficiency in \mathcal{B} and f_L are estimated by varying the efficiency by $\pm 1\sigma$. The statistical uncertainty of the efficiency due to the MC sample size is included in the systematic uncertainty.

The uncertainty due to the single candidate selection is estimated by comparing the results with a random candidate selection and with the nominal one. The fractions of SCF events are fixed to the MC expectation and we treat the deviation from the nominal value as the uncertainty, with the mean of \mathcal{B} and f_L obtained from MC ensemble tests varying SCF fraction to the signal by $\pm 20\%$. The uncertainties due to peaking backgrounds are evaluated by changing their yields by the fractional uncertainties in their branching fractions, as listed in Table III. The uncertainties due to the yields of $\tau^+\tau^-$ backgrounds are evaluated by varying these yields by $\pm 100\%$ from their nominal values (obtained from MC simulation), as the phase-space distribution of many of these modes is unknown (e.g., the dominant mode $\tau^- \rightarrow \pi^-\pi^+\pi^-\pi^0\nu_\tau$).

The uncertainties due to the signal, $q\bar{q}$, $B\bar{B}$, $\tau^+\tau^-$, and peaking background modeling are estimated by changing the PDF shape parameters by their uncertainties. The peak positions and widths for ΔE and $m_{\pi^\pm\pi^0}$ are calibrated using a $B^+ \rightarrow \bar{D}^0\rho^+$ sample. The shifts in peak positions and the data-simulation ratios of the width are -7.6 ± 0.46 MeV, 1.141 ± 0.015 for the ΔE distribution, and -9.82 ± 0.67 MeV/ c^2 , 1.025 ± 0.014 for the $m_{\pi^\pm\pi^0}$ distribution. We also include the uncertainty in the PDF shapes due to the limited MC sample size. The uncertainties due to interference with $B^0 \rightarrow \pi^+\pi^-\pi^0\pi^0$, $B^+ \rightarrow \rho^\pm\pi^\mp\pi^0$, $B^0 \rightarrow a_1^0\pi^0$, and $B^0 \rightarrow a_1^\pm\pi^\mp$ decays, which have the same final-state particles as $B^0 \rightarrow \rho^+\rho^-$, is evaluated using simulated datasets, changing the strong phases relative to the signal from zero to 2π radians assuming the branching fractions of the background modes to be 10^{-5} . We repeat the fits with different interference samples and take the

standard deviation of the results as the uncertainty.

The systematic uncertainty due to the mis-modeling of MC samples is estimated by changing the $\cos\theta_{\rho^\pm}$ PDF for the combinatorial $B\bar{B}$ and $q\bar{q}$ backgrounds by the differences observed between MC and data events in the M_{bc} sideband. We estimate the effect of mis-modeling in the $\cos\theta_{\rho^\pm}$ PDF for signal and peaking backgrounds by varying the PDFs by their MC-data differences as measured for the $B^\pm \rightarrow D^0\rho^\pm$ control sample.

To check for a possible fit bias, we perform an ensemble test using the MC-simulated samples. The observed bias is included as a systematic uncertainty. The uncertainty due to $N_{B\bar{B}}$ is included, as well as the uncertainty in f_{+-}/f_{00} obtained in Ref.[50].

Table VI. Systematic uncertainties for \mathcal{B} and f_L . Relative uncertainties are shown for \mathcal{B} .

| Source | \mathcal{B} [%] | f_L [10^{-2}] |
|---|-------------------|---------------------|
| Tracking | ± 0.54 | — |
| π^0 efficiency | ± 7.67 | — |
| PID | ± 0.08 | — |
| \mathcal{T}_C | ± 2.87 | — |
| MC sample size | ± 0.24 | ± 0.2 |
| Single candidate selection | ± 0.55 | ± 0.3 |
| SCF ratio | +2.97 -2.45 | +0.2 -0.3 |
| \mathcal{B} 's of peaking backgrounds | +0.94 -0.98 | ± 0.1 |
| $\tau^+\tau^-$ background yield | +0.65 -0.69 | ± 0.0 |
| Signal model | +1.14 -2.02 | ± 0.2 |
| $q\bar{q}$ model | +0.49 -0.51 | +0.1 -0.2 |
| $B\bar{B}$ model | +1.00 -0.40 | +0.3 -0.1 |
| $\tau^+\tau^-$ model | +0.17 -0.26 | +0.0 -0.1 |
| Peaking model | +1.37 -1.01 | +0.3 -0.5 |
| Interference | ± 1.20 | ± 0.5 |
| Data-MC mis-modeling | +3.51 -1.70 | +0.8 -0.3 |
| Fit bias | ± 1.03 | ± 1.2 |
| f_{+-}/f_{00} | ± 1.51 | — |
| $N_{B\bar{B}}$ | ± 1.45 | — |
| Total systematic uncertainty | +10.07 -9.51 | +1.7 -1.5 |
| Statistical uncertainty | +7.93 -7.58 | +2.4 -2.5 |

B. Time-Dependent CP-asymmetry fit

Table VII summarizes the statistical and systematic uncertainties of the time-dependent CP -asymmetry fit. The systematic uncertainties due to sources that contribute to both the signal extraction and CP asymmetry fits are obtained by repeating the signal extraction fit as described in Section VIA, and then repeating the CP asymmetry fit with the modified signal fraction. The following uncertainties are included: branching fractions for peaking backgrounds, $\tau^+\tau^-$ yields, mis-modeling of MC samples, single candidate selection, the SCF ratio,

signal and background modeling, fit bias, and interference.

We estimate the systematic uncertainty due to the resolution function by changing the resolution function parameters one by one by the uncertainties resulting from the $B^0 \rightarrow D^{*-} \pi^+$ calibration procedure. For parameters that are not calibrated, we allow them to float in the fit and take the resulting shifts in S and C as the systematic uncertainties.

We validate the Δt PDF shapes for $B\bar{B}$ and $q\bar{q}$ backgrounds by performing a fit to events in the M_{bc} -sideband region. The systematic uncertainty associated with these Δt PDF shapes is estimated by varying the shape parameters in the Delta t PDF for $B\bar{B}$ and $q\bar{q}$ backgrounds and repeating the fit.

The interference between CKM-favored and CKM-suppressed tag-side decays affects the values of S and C measured on the signal side [53]. We generate simulated datasets both with and without interference effects and take the shifts in the values of S and C as the systematic uncertainties.

The wrong-tag fractions are calibrated as described in Ref. [44]. We estimate the uncertainty due to these wrong-tag fractions by varying the fractions by their uncertainties and repeating the fits. The resulting changes in the fit results from the nominal values are taken as the systematic uncertainties.

The values listed in Table IV allow for possible CP violation in the peaking backgrounds. We generate simulated datasets varying the CP violating parameters for the backgrounds one at a time. The systematic uncertainty is estimated by taking the quadratic sum of the observed shifts. We estimate the uncertainty due to possible CP violation in the TP signal in the same way, considering 50% CP violation in TP signal events and taking $f_L = 0.92$.

We estimate the uncertainty due to possible misalignment of the tracking detector [54]. We reconstruct a simulated sample for $B^0 \rightarrow \rho^+ \rho^-$ assuming four detector misalignment scenarios and extract S and C . The systematic uncertainty is taken to be the maximum deviation from the nominal values. We estimate the systematic uncertainty due to fixed physics parameters τ_{B^0} and Δm_d by varying them by their uncertainties [12].

C. Correlation

Table VIII summarizes the correlations among the four results for the statistical and systematic uncertainties. We first estimate the correlations for each uncertainty individually. For example, we vary the PDF shape parameters by their uncertainties and record the changes for each pair of measurements to estimate the correlation of the modeling. This procedure is applied to all sources of systematics. The fitter gives the correlation of the statistical uncertainty between \mathcal{B} and f_L , as well as between S and C . The statistical correlation between \mathcal{B}

Table VII. Systematic uncertainties for S and C .

| Source | $S[10^{-2}]$ | $C[10^{-2}]$ |
|--|--------------|--------------|
| \mathcal{B} 's of peaking backgrounds | +0.6 -0.5 | ± 0.1 |
| $\tau\tau$ background yield | ± 0.9 | +0.0 -0.1 |
| Data-MC mis-modeling | +0.6 -1.1 | +1.5 -0.6 |
| Single candidate selection | ± 1.3 | ± 1.9 |
| SCF ratio | +0.5 -0.4 | +0.7 -0.0 |
| Signal model | +1.1 -1.4 | +0.3 -0.4 |
| $q\bar{q}$ model | +2.2 -1.0 | ± 0.2 |
| $B\bar{B}$ model | ± 0.9 | +0.7 -0.5 |
| $\tau^+\tau^-$ model | ± 0.1 | ± 0.0 |
| Peaking model | +0.8 -0.4 | +0.2 -0.4 |
| Fit bias | ± 2.0 | ± 0.6 |
| Interference | ± 2.8 | ± 1.7 |
| Resolution | +3.4 -4.4 | +1.9 -1.4 |
| Δt PDF for $q\bar{q}$ and $B\bar{B}$ | +3.8 -1.8 | +0.7 -0.1 |
| Tag side interference | ± 0.5 | ± 2.1 |
| Wrong tag fraction | +0.2 -0.3 | ± 0.5 |
| Background CP violation | +3.8 -3.6 | +4.2 -3.7 |
| CP violation in TP signal | +0.8 -0.2 | +0.2 -0.4 |
| Tracking detector misalignment | ± 1.4 | ± 0.5 |
| τ_{B^0} and Δm_d | +1.4 -1.6 | ± 0.3 |
| Total systematic uncertainty | +8.2 -7.8 | +6.1 -5.3 |
| Statistical uncertainty | ± 18.8 | ± 12.1 |

or f_L and S or C is estimated by varying \mathcal{B} or f_L by 1σ and then repeating the CP fit.

Table VIII. The correlations among the measurements for the statistical and systematic uncertainties.

| Stat. | f_L | S | C |
|---------------|-------|-------|-------|
| \mathcal{B} | -0.11 | 0.04 | 0.01 |
| f_L | | 0.03 | 0.05 |
| S | | | -0.06 |
| Syst. | f_L | S | C |
| \mathcal{B} | -0.12 | 0.06 | 0.01 |
| f_L | | -0.03 | 0.00 |
| S | | | 0.02 |

VII. CONSTRAINTS ON THE CKM ANGLE ϕ_2

We extract ϕ_2 by performing an isospin analysis with the Gronau-London isospin relations [16],

$$\frac{1}{\sqrt{2}}A_{+-} + A_{00} = A_{+0}, \quad (16)$$

$$\frac{1}{\sqrt{2}}\bar{A}_{+-} + \bar{A}_{00} = \bar{A}_{-0}, \quad (17)$$

where A_{ij} is the amplitude of longitudinally polarized $B \rightarrow \rho^i \rho^j$. We use results from the Belle, BABAR, and

LHCb experiments for \mathcal{B} , f_L , and CP violation parameters for $B^0 \rightarrow \rho^+\rho^-$, $B^0 \rightarrow \rho^0\rho^0$, and $B^+ \rightarrow \rho^+\rho^0$ decays, and the ratio of B^+ and B^0 lifetimes as listed in the PDG [12]. Since Belle and BABAR assumed equal production of B^+B^- and $B^0\bar{B}^0$ pairs, we correct their \mathcal{B} values to account for the latest HFLAV value of f_{+-}/f_{00} [50]. The inclusion of this effect slightly increases the branching fractions for the B^0 mode and slightly decreases that for the B^+ mode. The result of the isospin analysis is $\phi_2 = (91.5^{+4.8}_{-5.2})^\circ$ and $\Delta\phi_2 = (2.4^{+4.2}_{-3.8})^\circ$. The updated value of f_{+-}/f_{00} shifts ϕ_2 by -0.4° .

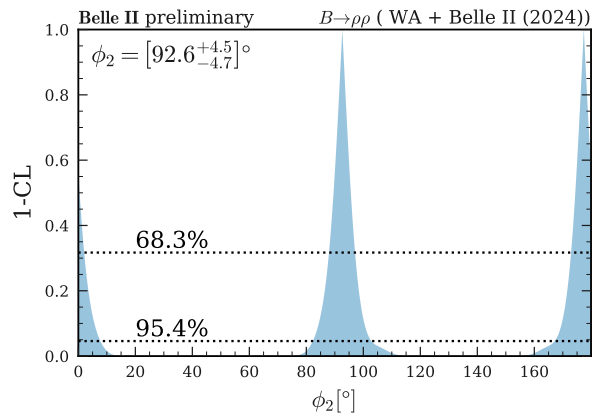


Fig. 4. Probability (1–Confidence-Level) for the CKM angle ϕ_2 based on combined inputs from the world averages [12] and our results of $B \rightarrow \rho\rho$ decays. The black dotted lines correspond to the 0.683 and 0.954 confidence levels.

We subsequently combine our $B^0 \rightarrow \rho^+\rho^-$ results with other results and extract ϕ_2 . The results are $\phi_2 = (92.6^{+4.5}_{-4.7})^\circ$ and $\Delta\phi_2 = (2.4^{+3.8}_{-3.7})^\circ$. The likelihood curve is shown in Figure 4. Our isospin analysis yields a second solution of $\phi_2 = (177.4^{+4.7}_{-4.5})^\circ$ and $\Delta\phi_2 = (-2.4^{+3.7}_{-3.8})^\circ$; however, this value for ϕ_2 is excluded by measurements of the UT angles ϕ_1 and ϕ_3 [12] and unitarity. The dominant uncertainties on ϕ_2 are due to the S parameters for $B^0 \rightarrow \rho^+\rho^-$ and $B^0 \rightarrow \rho^0\rho^0$.

VIII. CONCLUSIONS

We have measured the branching fraction and longitudinal polarization fraction for $B^0 \rightarrow \rho^+\rho^-$ decays as well as CP violation parameters for the longitudinal polarized decay using a data sample of $(387 \pm 6) \times 10^6 B\bar{B}$ pairs. We obtain

$$\mathcal{B}(B^0 \rightarrow \rho^+\rho^-) = (2.88^{+0.23+0.29}_{-0.22-0.27}) \times 10^{-5}, \quad (18)$$

$$f_L = 0.921^{+0.024+0.017}_{-0.025-0.015}, \quad (19)$$

$$S = -0.26 \pm 0.19 \pm 0.08, \quad (20)$$

$$C = -0.02 \pm 0.12^{+0.06}_{-0.05}, \quad (21)$$

where the first uncertainties are statistical and the second are systematic. The Belle II results are in good

agreement with previous measurements [18, 19]. We constrain ϕ_2 using our results as well as $B \rightarrow \rho\rho$ results from other experiments and include the effect of f_{+-}/f_{00} differing from unity. We obtain $\phi_2 = (92.6^{+4.5}_{-4.7})^\circ$, which is consistent with other UT observables. The uncertainty is dominated by the precision of the S parameters for $B^0 \rightarrow \rho^+\rho^-$ and $B^0 \rightarrow \rho^0\rho^0$, which can be improved by future measurements. This result can be used to constrain non-SM physics.

ACKNOWLEDGEMENTS

This work, based on data collected using the Belle II detector, which was built and commissioned prior to March 2019, was supported by Higher Education and Science Committee of the Republic of Armenia Grant No. 23LCG-1C011; Australian Research Council and Research Grants No. DP200101792, No. DP210101900, No. DP210102831, No. DE220100462, No. LE210100098, and No. LE230100085; Austrian Federal Ministry of Education, Science and Research, Austrian Science Fund No. P 34529, No. J 4731, No. J 4625, and No. M 3153, and Horizon 2020 ERC Starting Grant No. 947006 “InterLeptons”; Natural Sciences and Engineering Research Council of Canada, Compute Canada and CANARIE; National Key R&D Program of China under Contract No. 2022YFA1601903, National Natural Science Foundation of China and Research Grants No. 11575017, No. 11761141009, No. 11705209, No. 11975076, No. 12135005, No. 12150004, No. 12161141008, No. 12475093, and No. 12175041, and Shandong Provincial Natural Science Foundation Project ZR2022JQ02; the Czech Science Foundation Grant No. 22-18469S and Charles University Grant Agency project No. 246122; European Research Council, Seventh Framework PIEF-GA-2013-622527, Horizon 2020 ERC-Advanced Grants No. 267104 and No. 884719, Horizon 2020 ERC-Consolidator Grant No. 819127, Horizon 2020 Marie Skłodowska-Curie Grant Agreement No. 700525 “NIOBE” and No. 101026516, and Horizon 2020 Marie Skłodowska-Curie RISE project JENNIFER2 Grant Agreement No. 822070 (European grants); L’Institut National de Physique Nucléaire et de Physique des Particules (IN2P3) du CNRS and L’Agence Nationale de la Recherche (ANR) under grant ANR-21-CE31-0009 (France); BMBF, DFG, HGF, MPG, and AvH Foundation (Germany); Department of Atomic Energy under Project Identification No. RTI 4002, Department of Science and Technology, and UPES SEED funding programs No. UPES/R&D-SEED-INFRA/17052023/01 and No. UPES/R&D-SOE/20062022/06 (India); Israel Science Foundation Grant No. 2476/17, U.S.-Israel Binational Science Foundation Grant No. 2016113, and Israel Ministry of Science Grant No. 3-16543; Istituto Nazionale di Fisica Nucleare and the Research Grants BELLE2; Japan Society for the Promotion of Science, Grant-in-Aid for Scientific

Research Grants No. 16H03968, No. 16H03993, No. 16H06492, No. 16K05323, No. 17H01133, No. 17H05405, No. 18K03621, No. 18H03710, No. 18H05226, No. 19H00682, No. 20H05850, No. 20H05858, No. 22H00144, No. 22K14056, No. 22K21347, No. 23H05433, No. 26220706, and No. 26400255, and the Ministry of Education, Culture, Sports, Science, and Technology (MEXT) of Japan; National Research Foundation (NRF) of Korea Grants No. 2016R1-D1A1B-02012900, No. 2018R1-A6A1A-06024970, No. 2021R1-A6A1A-03043957, No. 2021R1-F1A-1060423, No. 2021R1-F1A-1064008, No. 2022R1-A2C-1003993, No. 2022R1-A2C-1092335, No. RS-2023-00208693, No. RS-2024-00354342 and No. RS-2022-00197659, Radiation Science Research Institute, Foreign Large-Size Research Facility Application Supporting project, the Global Science Experimental Data Hub Center, the Korea Institute of Science and Technology Information (K24L2M1C4) and KREONET/GLORIAD; Universiti Malaya RU grant, Akademi Sains Malaysia, and Ministry of Education Malaysia; Frontiers of Science Program Contracts No. FOINS-296, No. CB-221329, No. CB-236394, No. CB-254409, and No. CB-180023, and SEP-CINVESTAV Research Grant No. 237 (Mexico); the Polish Ministry of Science and Higher Education and the National Science Center; the Ministry of Science and Higher Education of the Russian Federation and the HSE University Basic Research Program, Moscow; University of Tabuk Research Grants No. S-0256-1438 and No. S-0280-1439 (Saudi Arabia), and King Saud University, Riyadh, Researchers Supporting Project number (RSPD2024R873) (Saudi Arabia); Slovenian Research Agency and Research Grants No. J1-9124

and No. P1-0135; Agencia Estatal de Investigacion, Spain Grant No. RYC2020-029875-I and Generalitat Valenciana, Spain Grant No. CIDEAGENT/2018/020; The Knut and Alice Wallenberg Foundation (Sweden), Contracts No. 2021.0174 and No. 2021.0299; National Science and Technology Council, and Ministry of Education (Taiwan); Thailand Center of Excellence in Physics; TUBITAK ULAKBIM (Turkey); National Research Foundation of Ukraine, Project No. 2020.02/0257, and Ministry of Education and Science of Ukraine; the U.S. National Science Foundation and Research Grants No. PHY-1913789 and No. PHY-2111604, and the U.S. Department of Energy and Research Awards No. DE-AC06-76RLO1830, No. DE-SC0007983, No. DE-SC0009824, No. DE-SC0009973, No. DE-SC0010007, No. DE-SC0010073, No. DE-SC0010118, No. DE-SC0010504, No. DE-SC0011784, No. DE-SC0012704, No. DE-SC0019230, No. DE-SC0021274, No. DE-SC0021616, No. DE-SC0022350, No. DE-SC0023470; and the Vietnam Academy of Science and Technology (VAST) under Grants No. NVCC.05.12/22-23 and No. DL0000.02/24-25.

These acknowledgements are not to be interpreted as an endorsement of any statement made by any of our institutes, funding agencies, governments, or their representatives.

We thank the SuperKEKB team for delivering high-luminosity collisions; the KEK cryogenics group for the efficient operation of the detector solenoid magnet and IBelle on site; the KEK Computer Research Center for on-site computing support; the NII for SINET6 network support; and the raw-data centers hosted by BNL, DESY, GridKa, IN2P3, INFN, and the University of Victoria.

-
- [1] N. Cabibbo, Phys. Rev. Lett. **10**, 531 (1963).
 [2] M. Kobayashi and T. Maskawa, Prog. Theor. Phys. **49**, 652 (1973).
 [3] <http://www.utfit.org/UTfit/WebHome>.
 [4] J. Charles, A. Höcker, H. Lacker, S. Laplace, F. R. Le Diberder, J. Malclés, J. Ocariz, M. Pivk, and L. Roos, The European Physical Journal C **41**, 1–131 (2005), updated results and plots available at: <http://ckmfitter.in2p3.fr>.
 [5] M. Bona *et al.* (UTfit Collaboration), JHEP **03**, 049 (2008), arXiv:0707.0636 [hep-ph].
 [6] W. Altmannshofer, R. Harnik, and J. Zupan, JHEP **11**, 202 (2013), arXiv:1308.3653 [hep-ph].
 [7] A. J. Buras and J. Girrbach, Rept. Prog. Phys. **77**, 086201 (2014), arXiv:1306.3775 [hep-ph].
 [8] M. Tanimoto and K. Yamamoto, Phys. Lett. B **735**, 426 (2014), arXiv:1404.0520 [hep-ph].
 [9] J. Charles *et al.*, Phys. Rev. D **91**, 073007 (2015), arXiv:1501.05013 [hep-ph].
 [10] J. Charles, S. Descotes-Genon, Z. Ligeti, S. Monteil, M. Papucci, K. Trabelsi, and L. Vale Silva, Phys. Rev. D **102**, 056023 (2020).
 [11] The angle ϕ_2 is also known as α .
 [12] S. Navas *et al.* (Particle Data Group), Phys. Rev. **D110**, 030001 (2024).
 [13] We use a system of units in which $c = \hbar = 1$.
 [14] The CP violation parameter C is also defined as $A = -C$.
 [15] We assume no CP violation in B^0 - \bar{B}^0 mixing, which is an excellent approximation.
 [16] M. Gronau and D. London, Phys. Rev. Lett. **65**, 3381 (1990).
 [17] Throughout this paper, the inclusion of the charge conjugate decay mode is implied unless otherwise specified.
 [18] B. Aubert *et al.* (BaBar Collaboration), Phys. Rev. D **76**, 052007 (2007), arXiv:0705.2157 [hep-ex].
 [19] P. Vanhoefer *et al.* (Belle Collaboration), Phys. Rev. D **93**, 032010 (2016), [Addendum: Phys.Rev.D 94, 099903 (2016)], arXiv:1510.01245 [hep-ex].
 [20] J. Zhang *et al.* (Belle Collaboration), Phys. Rev. Lett. **91**, 221801 (2003), arXiv:hep-ex/0306007.
 [21] B. Aubert *et al.* (BaBar Collaboration), Phys. Rev. Lett. **97**, 261801 (2006), arXiv:hep-ex/0607092.
 [22] B. Aubert *et al.* (BaBar Collaboration), Phys. Rev. D **78**, 071104 (2008), arXiv:0807.4977 [hep-ex].

- [23] I. Adachi *et al.* (Belle Collaboration), Phys. Rev. D **89**, 072008 (2014), [Addendum: Phys.Rev.D 89, 119903 (2014)], arXiv:1212.4015 [hep-ex].
- [24] R. Aaij *et al.* (LHCb Collaboration), Phys. Lett. B **747**, 468 (2015), arXiv:1503.07770 [hep-ex].
- [25] J. Charles, O. Deschamps, S. Descotes-Genon, and V. Niess, Eur. Phys. J. C **77**, 574 (2017), arXiv:1705.02981 [hep-ph].
- [26] I. Adachi *et al.* (Belle II Collaboration), (2024), arXiv:2407.00965 [hep-ex].
- [27] T. Abe (Belle II Collaboration), (2010), arXiv:1011.0352 [physics.ins-det].
- [28] K. Akai, K. Furukawa, and H. Koiso, Nucl. Instrum. Meth. **A907**, 188 (2018), arXiv:1809.01958 [physics.acc-ph].
- [29] K. Adamczyk *et al.* (Belle II SVD Group), JINST **17**, P11042 (2022), arXiv:2201.09824 [physics.ins-det].
- [30] D. Kotchetkov *et al.*, Nucl. Instrum. Meth. A **941**, 162342 (2019), arXiv:1804.10782 [physics.ins-det].
- [31] D. J. Lange, *Proceedings, 7th International Conference on B physics at hadron machines (BEAUTY 2000): Maagan, Israel, September 13-18, 2000*, Nucl. Instrum. Meth. **A462**, 152 (2001).
- [32] S. Jadach, B. F. L. Ward, and Z. Wąs, Comput. Phys. Commun. **130**, 260 (2000), arXiv:hep-ph/9912214 [hep-ph].
- [33] T. Sjöstrand, S. Ask, J. R. Christiansen, R. Corke, N. Desai, P. Ilten, S. Mrenna, S. Prestel, C. O. Rasmussen, and P. Z. Skands, Comput. Phys. Commun. **191**, 159 (2015), arXiv:1410.3012 [hep-ph].
- [34] T. Skwarnicki, *A study of the radiative CASCADE transitions between the Upsilon-Prime and Upsilon resonances*, Ph.D. thesis, Cracow, INP (1986).
- [35] E. Barberio and Z. Wąs, Comput. Phys. Commun. **79**, 291 (1994).
- [36] S. Agostinelli *et al.* (GEANT4 Collaboration), Nucl.Instrum.Meth. **A506**, 250 (2003).
- [37] P. M. Lewis *et al.*, Nucl. Instrum. Meth. A **914**, 69 (2019), arXiv:1802.01366 [physics.ins-det].
- [38] Z. J. Liptak *et al.*, Nucl. Instrum. Meth. A **1040**, 167168 (2022), arXiv:2112.14537 [physics.ins-det].
- [39] T. Kuhr, C. Pulvermacher, M. Ritter, T. Hauth, and N. Braun (Belle II Framework Software Group), Comput. Softw. Big Sci. **3**, 1 (2019), arXiv:1809.04299 [physics.comp-ph].
- [40] Belle II Collaboration, “Belle II Analysis Software Framework (basf2),” <https://doi.org/10.5281/zenodo.5574115>.
- [41] T. Keck, Computing and Software for Big Science **1**, 2 (2017).
- [42] J.-F. Krohn *et al.* (Belle II Analysis Software Group), Nucl. Instrum. Meth. **A976**, 164269 (2020), arXiv:1901.11198 [hep-ex].
- [43] F. Abudinén *et al.* (Belle II Collaboration), Phys. Rev. D **107**, L091102 (2023), arXiv:2302.12791 [hep-ex].
- [44] I. Adachi *et al.* (Belle II Collaboration), Phys. Rev. D **110**, 012001 (2024), arXiv:2402.17260 [hep-ex].
- [45] S. O. Arik and T. Pfister, “Tabnet: Attentive interpretable tabular learning,” (2020), arXiv:1908.07442 [cs.LG].
- [46] S. Brandt, C. Peyrou, R. Sosnowski, and A. Wroblewski, Phys. Lett. **12**, 57 (1964).
- [47] G. C. Fox and S. Wolfram, Phys. Rev. Lett. **41**, 1581 (1978).
- [48] S. H. Lee *et al.* (Belle Collaboration), Phys. Rev. Lett. **91**, 261801 (2003), arXiv:hep-ex/0308040.
- [49] R. Storn and K. Price, Journal of Global Optimization **11**, 341 (1997).
- [50] S. Banerjee *et al.*, “Averages of b -hadron, c -hadron, and τ -lepton properties as of 2023,” (2024), arXiv:2411.18639 [hep-ex].
- [51] J. M. Blatt and V. F. Weisskopf, *Theoretical nuclear physics* (Springer, New York, 1952).
- [52] M. Pivk and F. R. Le Diberder, Nucl. Instrum. Meth. **A555**, 356 (2005), arXiv:physics/0402083 [physics.data-an].
- [53] O. Long, M. Baak, R. N. Cahn, and D. Kirkby, Physical Review D **68** (2003), 10.1103/physrevd.68.034010.
- [54] T. Bilka *et al.*, EPJ Web Conf. **245**, 02023 (2020).